PERGAMON

International Journal of Heat and Mass Transfer 44 (2001) 2029–2042

International Journal of HEAT and MASS TRANSFER

www.elsevier.com/locate/ijhmt

Numerical prediction of mass-exchange between cathode and anode channels in a PEM fuel cell

Sandip Dutta [a,*], Sirivatch Shimpalee [a], J.W. Van Zee [b]

[a] *Department of Mechanical Engineering, University of South Carolina, 300S. Main Street, Columbia, SC 29208, USA*
[b] *Department of Chemical Engineering, University of South Carolina, Columbia, SC 29208, USA*

Received 19 October 1999; received in revised form 20 July 2000

Abstract

A numerical model is developed to predict the mass flow between channels in a Polymer Electrolyte Membrane (PEM) fuel cell with a serpentine flow path. The complete three-dimensional Navier–Stokes equations with multi-species mixture are solved and electro-chemical reactions are modeled as mass source/sink terms in the control volumes. The results indicate that flow distribution in both anode and cathode channels are significantly affected by the mass consumption patterns on the Membrane Electrode Assembly (MEA). The water transport is governed by both electro-osmosis and diffusion processes. Further, the overall pressure drop is less than that expected for a regular straight channel flow.

1. Introduction

The Polymer Electrolyte Membrane (PEM) fuel cell operates at significantly lower temperatures than other types of fuel cells and is a strong candidate to be the power source of future generation automobiles. In a typical fuel cell, hydrogen fuel indirectly reacts with oxygen to produce electrical power and the byproduct of the energy conversion process is water. The PEM fuel cell commonly has main channel flow paths grooved in graphite current collectors and reacting gases that reach the catalyst laden electrode assembly through a porous diffusion layer. The extent to which mass is transported in this porous layer may help explain some interesting characteristics recently revealed in experimental studies [1]. In this work, numerical predictions of flow and mass transfer of individual gases are analyzed with the aid of new computation methods. So far, no experimental data are available to validate our flow predictions. However, the current density predictions by our model have been favorably compared with experimental data as discussed in Shimpalee et al. [1].

In a typical PEM fuel cell, gas diffusion layers are used to enhance the reaction area accessible by the reactants. These diffusion layers allow a spatial distribution in the current density on the membrane in both the direction of bulk flow and the direction orthogonal to the flow but parallel to the membrane. This two-dimensional distribution cannot be modeled with the conventional one and two-dimensional models such as those shown in [2–7], as discussed recently by Dutta et al. [8]. The key requirement for prediction of this distribution is that one account for the effect of the width of the flow channel on the velocity distribution. Dutta et al. [8] reported a numerical model that includes the three-dimensional solution to the Navier–Stokes equations for a straight flow channel PEM and they discussed how the mass consumed in the electro-chemical reactions affects the momentum transport equations. Here, we extend their work by modeling a complete fuel cell with the serpentine flow field shown in Fig. 1.

In this work, we present the numerical predictions of the velocity distribution, the gas-mixture distribution, and the detailed reactant consumption on the membrane electrode assembly (MEA). Predictions of the water source and sink terms on the two sides of the membrane show that for the operating conditions considered, the electro-osmotic drag of water is usually greater than the

* Corresponding author. Tel.: +1-803-777-8013; fax: +1-803-777-0106.
E-mail address: dutta@engr.sc.edu (S. Dutta).

0017-9310/01/$ - see front matter
PII: S0017-9310(00)00257-X

Nomenclature

a_K	activity of water in stream K, dimensionless
A_{cv}	specific surface area of the control volume (cv) (m^{-1})
C_{wK}	concentration of water at K interface of the membrane (mol m^{-3})
D_h	hydraulic diameter of flow channel (m)
$D_{i,j}$	pseudo binary diffusion coefficient of species i in mixture j (m^2 s^{-1})
D_w	diffusion coefficient of water (m^2 s^{-1})
F	Faraday constant (96,487 C mole-of-electrons^{-1})
I	local current density (A m^{-2})
I_o	exchange current density for the oxygen reaction (100 A m^{-2})
L	length of the serpentine flow channel (m)
$m_{K,l}$	mass fraction of the species l in stream K, dimensionless
$M_{m,dry}$	equivalent weight of a dry membrane (kg mol^{-1})
M_{H_2}	molecular weight of hydrogen (kg mol^{-1})
M_{O_2}	molecular weight of oxygen (kg mol^{-1})
$P^{sat}_{w,K}$	vapor pressure of water in stream K (Pa)
P	pressure (Pa)
P_{O_2}	partial pressure of oxygen (Pa)
Q	volume flow rate (m^3 s^{-1})
R	universal gas constant (8.314 J mol^{-1} k^{-1})
t_m	membrane thickness (m)
T_s	surface temperature at the anode (K)
T_{cell}	fuel cell operating temperature
u, v, w	velocities in x, y, and z directions, respectively (m s^{-1})
V_{oc}	cell open-circuit voltage (V)
V_{cell}	cell voltage (V)
x	channel length measured from anode inlet (m)
$X_{w,K}$	mole fraction of water in stream K
μ	dynamic viscosity (kg s m^{-2})
α	net water flux per proton flux
λ	water content in the membrane
n_d	electro-osmotic drag coefficient (number of water molecules carried per proton)
η	overpotential for oxygen reaction (V)
σ_m	membrane conductivity (ohm^{-1} m^{-1})
$\rho_{m,dry}$	density of a dry membrane (kg m^{-3})
ρ	density of the mixture (kg m^{-3})
β_ξ	permeability in the ξ direction

Subscripts and superscripts

a	anode
c	cathode
H_2	hydrogen
K	anode or cathode
O_2	oxygen
w	water
sat	saturated
ξ	dummy variable for direction x, y, or z

back-diffusion. The simulation regions consist of two flow channels (anode and cathode) separated by the MEA. There are two diffusion layers, which are made of porous materials and are placed in between the flow channels and the MEA.

2. Model development

This numerical simulation is based on a steady state, single-phase, multi-species, isothermal, and three-dimensional mass transfer model of a full-cell PEM fuel cell. The actual flow path [9] consists of a serpentine gas channel that has 20 passes as shown in Fig. 1. Fig. 1 also shows the channel geometry and associated coordinate system. A thin MEA is sandwiched between anode and cathode diffusion layers and these diffusion layers can be compressed as the fuel cell is assembled (e.g., see [10]). Fig. 2 shows more details of the computational domain, which is composed of the anode flow channel, anode diffusion layer, MEA, cathode diffusion layer, and cathode flow channel. We consider four species: hydrogen, oxygen, nitrogen, and water vapor. The fuel cell operation is characterized as gas transport and the electrochemical transformation of hydrogen and oxygen species to the protons and water, respectively. The hydrogen from the anode flow channel is transported through the diffusion layer towards the membrane. Hydrogen molecules are dissociated to protons and electrons in the catalyst and the water that impregnates the MEA hydrates the protons. Protons travel to the cathode side of the MEA and convert oxygen to water. We assume that gas cannot permeate across the membrane. Water is transported across the membrane from the anode to the cathode by electro-osmosis and from the cathode to the anode by diffusion according to the activity gradients. The air mixture in the cathode channel is transported through the diffusion layer toward the membrane where oxygen reacts with protons. The water activity in the membrane is simulated by surface-based source terms in the control volumes in contact with the membrane.

2.1. Model equations

The conservation of mass equation (Table 1, Eq. (1)) in the three-dimensional flow solver software, FLU-

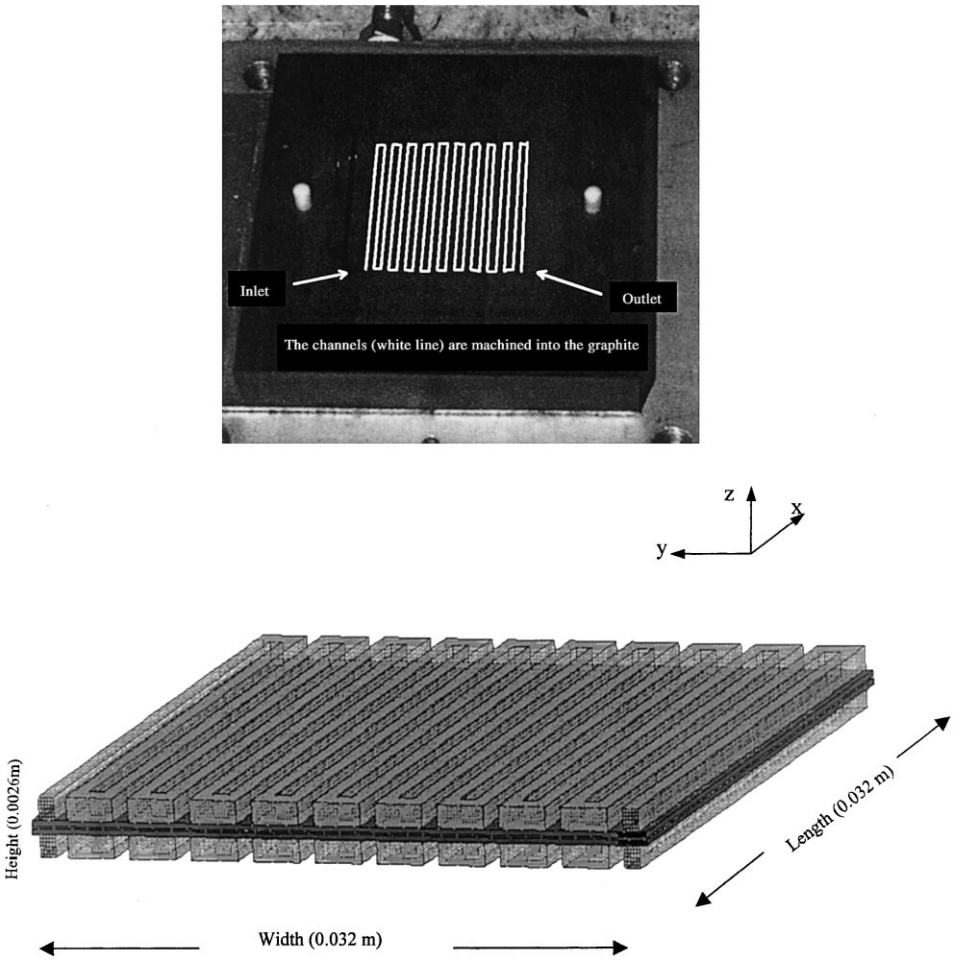

Fig. 1. The picture shows actual flow-field plate with the gas channels and its geometry model. There are 20 straight channels connected in a serpentine fashion. Anode-side and cathode-side flow channels are symmetric and placed properly aligned on top of each other [1].

ENT, is modified to include the electro-chemical aspects of a fuel cell by using the respective source terms, S_m, shown by Eqs. (7) and (10)–(12) of Table 1. Note that source terms are zero in most of the computation domain. These terms correspond to the consumption of hydrogen in the anode, the consumption of oxygen in the cathode, and production of water in the cathode. The flux of water is also included as a source term at the anode and cathode (i.e., Eqs. (10) and (12)) by accounting for the diffusion, water content in the membrane, and electro-osmotic drag coefficient as defined by Eqs. (16)–(18), respectively (see Table 2).

The momentum transport equation has a source term for the porous media used for flows through diffusion layer and it is based on Darcy's law [11]. The addition of this source term effectively converts the momentum equation in the x-direction to $(\partial P/\partial x) = -(\mu/\beta_x)u$ in the porous layer. Since β_x is very small, the other terms in the Navier–Stokes equation become negligible. A pressure drop is created in the porous layer that is proportional to the mixture velocity in the cell. The permeability, β_ξ, is assumed to be isotropic and is taken as 1.0×10^{-12} m^2.

The species transport equations (Eqs. (3)–(6) of Table 1) are solved to calculate the mass flow rates of the hydrogen, water, and oxygen based on the mixture velocities, $u, v,$ and w, and the diffusion mass fluxes $J_{\xi,1}$. The species binary diffusion coefficients are calculated as shown by Eq. (14) in Table 2. The mass flux of nitrogen was determined from a summation of the mass fractions of the other species. Fuller and Newman [3] integrated the flux expression for the diffusion of water through the membrane but we assumed a linear gradient as shown by Eq. (15) and as used in [4,5]. The flux of water through the membrane is critical to the current density predictions, and local current density

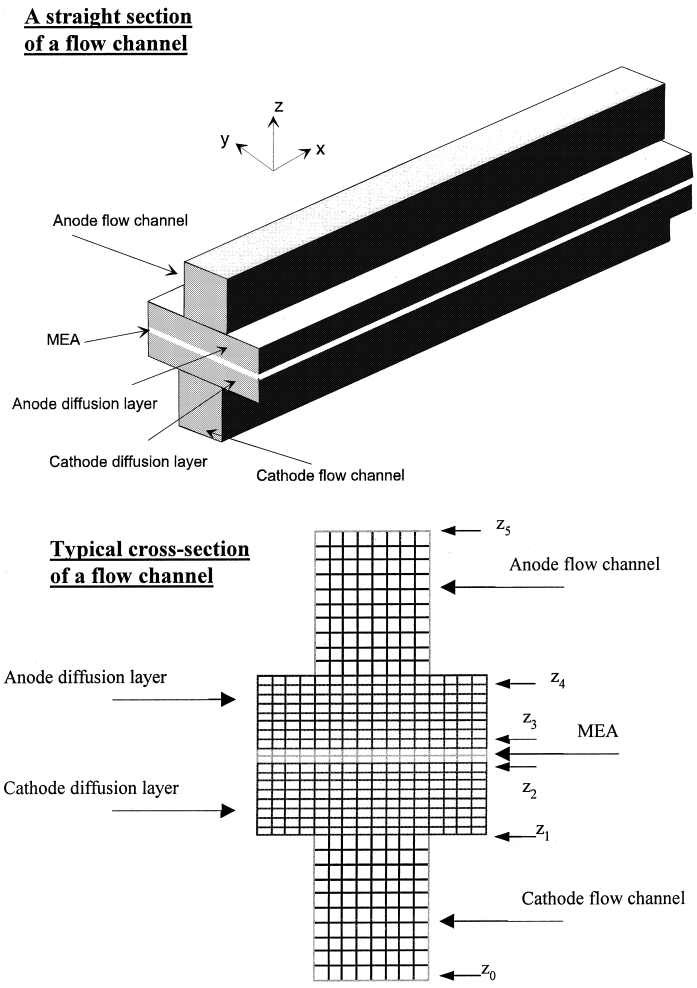

Fig. 2. The details of computational domain and grid arrangement used in this model [8].

governs local mass transfer calculations. Eq. (17) gives the relationship between the electro-osmotic drag coefficient and water content in the membrane. This equation is developed by curve fitting the values of water content in the membrane and electro-osmotic drag coefficient as presented in [2]. The diffusion coefficient, given in Eq. (18), is a function developed by piecewise linear approximation of the exponential data plotted in [2].

The expressions for water concentration at the anode and cathode sides, $C_{w,a}$ and $C_{w,c}$, are calculated according to Eq. (19) and the activity of water is also defined in Table 2. It is important to note that the source terms in Table 1 correspond to the control volume and not the boundary conditions at the anode or cathode interfaces. For the correct determination of the concentrations and activities at the membrane–diffusion layer interface, the mole fraction for each species used in these equations are extrapolated to the membrane surface. We used linear extrapolation with the grid of Fig. 2 and achieved a grid independent solution.

2.2. Numerical procedure

A control volume technique based on a commercial flow solver, FLUENT (version 4.48), is used to solve the coupled governing equations. However, this software requires specification of the source terms shown in Table 1 and new subroutines are written to calculate the electro-chemical and permeability for this simulation. Also FLUENT requires a subroutine to account for the flux of protons and water across the membrane.

Fig. 2 shows that the geometry of fuel cell system consists of two flow channels (upper is anode and lower is cathode) separated by two diffusion layers and one MEA. There are 20 serpentine passes in the flow path, so that the flow path is approximately 60 cm long in the axial direction with 0.1 (height) $\times$ 0.08 (width) cm^2

Table 1
Governing equations and source terms

Governing equations	Mathematical expressions		Non-zero volumetric source terms and location of application (see Fig. 2)	
Conservation of mass	$\frac{\partial(\rho u)}{\partial x}+\frac{\partial(\rho v)}{\partial y}+\frac{\partial(\rho w)}{\partial z}=S_{\mathrm{m}}$	(1)	$S_{\mathrm{m}}=S_{\mathrm{H_2}}+S_{\mathrm{aw}}$ at $z=z_3$ $S_{\mathrm{m}}=S_{\mathrm{O_2}}+S_{\mathrm{cw}}$ at $z=z_2$	(7)
Momentum transport	$u\frac{\partial(\rho u)}{\partial x}+v\frac{\partial(\rho u)}{\partial y}+w\frac{\partial(\rho u)}{\partial z}=-\frac{\partial P}{\partial x}+\frac{\partial}{\partial x}\left(\mu\frac{\partial u}{\partial x}\right)+\frac{\partial}{\partial y}\left(\mu\frac{\partial u}{\partial y}\right)+\frac{\partial}{\partial z}\left(\mu\frac{\partial u}{\partial z}\right)+S_{px}$ $u\frac{\partial(\rho v)}{\partial x}+v\frac{\partial(\rho v)}{\partial y}+w\frac{\partial(\rho v)}{\partial z}=-\frac{\partial P}{\partial y}+\frac{\partial}{\partial x}\left(\mu\frac{\partial v}{\partial x}\right)+\frac{\partial}{\partial y}\left(\mu\frac{\partial v}{\partial y}\right)+\frac{\partial}{\partial z}\left(\mu\frac{\partial v}{\partial z}\right)+S_{py}$ $u\frac{\partial(\rho w)}{\partial x}+v\frac{\partial(\rho w)}{\partial y}+w\frac{\partial(\rho w)}{\partial z}=-\frac{\partial P}{\partial z}+\frac{\partial}{\partial x}\left(\mu\frac{\partial w}{\partial x}\right)+\frac{\partial}{\partial y}\left(\mu\frac{\partial w}{\partial y}\right)+\frac{\partial}{\partial z}\left(\mu\frac{\partial w}{\partial z}\right)+S_{pz}$	(2)	$S_{px}=-\frac{\mu u}{\beta_x}$; $S_{py}=-\frac{\mu v}{\beta_y}$; $S_{pz}=-\frac{\mu w}{\beta_z}$ at $z_1\leqslant z\leqslant z_4$	(8)
Hydrogen transport (anode side)	$u\frac{\partial(\rho m_{\mathrm{H_2}})}{\partial x}+v\frac{\partial(\rho m_{\mathrm{H_2}})}{\partial y}+w\frac{\partial(\rho m_{\mathrm{H_2}})}{\partial z}=\frac{\partial(J_{x,\mathrm{H_2}})}{\partial x}+\frac{\partial(J_{y,\mathrm{H_2}})}{\partial y}+\frac{\partial(J_{z,\mathrm{H_2}})}{\partial z}+S_{\mathrm{H_2}}$	(3)	$S_{\mathrm{H_2}}=-\frac{I(x,y)}{2F}M_{\mathrm{H_2}}A_{\mathrm{cv}}$ at $z=z_3$	(9)
Water transport (anode side)	$u\frac{\partial(m_{\mathrm{aw}})}{\partial x}+v\frac{\partial(\rho m_{\mathrm{aw}})}{\partial y}+w\frac{\partial(\rho m_{\mathrm{aw}})}{\partial z}=\frac{\partial(J_{x,\mathrm{aw}})}{\partial x}+\frac{\partial(J_{y,\mathrm{aw}})}{\partial y}+\frac{\partial(J_{z,\mathrm{aw}})}{\partial z}+S_{\mathrm{aw}}$	(4)	$S_{\mathrm{aw}}=-\frac{\alpha(x,y)}{F}I(x,y)M_{\mathrm{H_2O}}A_{\mathrm{cv}}$ at $z=z_3$	(10)
Oxygen transport (cathode side)	$u\frac{\partial(\rho m_{\mathrm{O_2}})}{\partial x}+v\frac{\partial(\rho m_{\mathrm{O_2}})}{\partial y}+w\frac{\partial(\rho m_{\mathrm{O_2}})}{\partial z}=\frac{\partial(J_{x,\mathrm{O_2}})}{\partial x}+\frac{\partial(J_{y,\mathrm{O_2}})}{\partial y}+\frac{\partial(J_{z,\mathrm{O_2}})}{\partial z}+S_{\mathrm{O_2}}$	(5)	$S_{\mathrm{O_2}}=-\frac{I(x,y)}{4F}M_{\mathrm{O_2}}A_{\mathrm{cv}}$ at $z=z_2$	(11)
Water transport (cathode side)	$u\frac{\partial(\rho m_{\mathrm{cw}})}{\partial x}+v\frac{\partial(\rho m_{\mathrm{cw}})}{\partial y}+w\frac{\partial(\rho m_{\mathrm{cw}})}{\partial z}=\frac{\partial(J_{x,\mathrm{cw}})}{\partial x}+\frac{\partial(J_{y,\mathrm{cw}})}{\partial y}+\frac{\partial(J_{y,\mathrm{cw}})}{\partial y}+S_{\mathrm{cw}}$	(6)	$S_{\mathrm{cw}}=\frac{1+2\alpha(x,y)}{2F}I(x,y)M_{\mathrm{H_2O}}A_{\mathrm{cv}}$ at $z=z_2$	(12)

Table 2
Equations for modeling electro-chemical effects

Diffusion mass flux of species l in ξ direction	$J_{i,l} = -\rho D_{i,l} \frac{\partial m_{K,l}}{\partial \xi}$	(13)
Binary diffusion coefficient [11]	$\frac{PD_{i,j}(x,y)}{(P_{c-i} * P_{c-j})^{1/3}(T_{c-i}T_{c-j})^{5/12}(\frac{1}{M_i}+\frac{1}{M_j})^{1/2}} = 3.64\times10^{-8}\left(\frac{T_{cell}}{\sqrt{T_{c-i}T_{c-j}}}\right)^{2.334}$	(14)
Net water transfer coefficient per proton	$\alpha(x,y) = n_d(x,y) - \frac{F}{I(x,y)} D_W(x,y) \frac{(C_{wc}(x,y) - C_{wa}(x,y))}{t_m}$	(15)
Water content in the membrane	$\lambda = 0.043 + 17.81a_a - 39.85a_a^2 + 36.0a_a^3;$ $0 < a_a \leqslant 1 = 14 + 1.4(a_a - 1); 1 < a_a \leqslant 3$	(16)
Electro-osmotic drag coefficient	$n_d = 0.0029\lambda^2 + 0.05\lambda - 3.4\times10^{-19}$	(17)
Water diffusion coefficient	$D_W = D_\lambda \exp\left(2416\left(\frac{1}{303} - \frac{1}{T_{cell}}\right)\right); \quad D_\lambda = 10^{-10}, \lambda < 2;$ $D_\lambda = 10^{-10}(1 + 2(\lambda - 2)), 2 \leqslant \lambda \leqslant 3;$ $D_\lambda = 10^{-10}(3 - 1.67(\lambda - 3)), 3 < \lambda < 4.5; \quad D_\lambda = 1.25\times10^{-10}, \ \lambda \geqslant 4.5$	(18)
Water concentration for anode and cathode surfaces of the MEA	$C_{wK}(x,y) = \frac{\rho_{m,dry}}{M_{m,dry}}(0.043 + 17.8a_K - 39.8a_K^2 + 36.0a_K^3);$ $a_K \leqslant 1 = \frac{\rho_{m,dry}}{M_{m,dry}}(14 + 1.4(a_K - 1)); \text{for } a_K > 1, \quad \text{where } K = a \text{ or } c$	(19)
Water activity	$a_K = \frac{X_{w,K}P(x,y)}{P_{w,K}^{sat}}$	(20)
Local current density	$I(x,y) = \frac{\sigma_m(x,y)}{t_m}\{V_{oc} - V_{cell} - \eta(x,y)\}$	(21)
Local membrane conductivity	$\sigma_m(x,y) = \left(0.00514\frac{M_{m,dry}}{\rho_{m,dry}}C_{wa}(x,y) - 0.00326\right)\exp\left(1268\left(\frac{1}{303} - \frac{1}{T_s}\right)\right)\times10^2$	(22)
Local overpotential	$\eta(x,y) = \frac{RT_s}{0.5F}\ln\left[\frac{I(x,y)P(x,y)}{I_o P_{O_2}(x,y)}\right]$	(23)
Viscosity of mixture	$\mu = \sum_i m_i \mu_i$	(24)

cross-section flow area. Each diffusion layer has dimension of 0.025 (height) × 3.20 (width) × 3.20 (length) cm^3. The total grid size of this fuel cell simulation is 34 × 200 × 28 uniform grid cells. The transport of water and proton is simulated by source terms in control volumes in contact with the membrane.

The solution procedure is based on SIMPLE [12] algorithm. Three momentum equations corresponding to three coordinates are solved, followed by a pressure correction equation that does the mass balance. Species transport equations are solved after the bulk flow calculation. The mixture properties at each control volume are calculated based on the local species content. The anode-side gas mixture contains hydrogen and water vapor. Whereas, the cathode-side gas mixture contains oxygen, water vapor, and nitrogen. Therefore, the density and viscosity of the two flow channels are different and vary from one location to the other. The computational domain has two inlets and two outlets with different gas-densities. To expedite convergence, a pressure outlet technique is used instead of an ordinary outlet condition. Moreover, since the density varies form location to location, a solution technique similar to compressible flow analysis is used to include these density variations.

3. Results and discussions

We present results for cases where the operating pressure is 202 kPa absolute and the cell temperature is constant at 343 K. We simulate four different inlet humidity conditions used by Lee et al. [9] as shown in Table 3. The thickness of the MEA used for these simulations is 100 μm and the cell voltage is set to 0.6 V. Figs. 3(a) and (b) show the anode and cathode-side flow vectors and density contours at two different locations of the fuel cell with very low humidity inlet conditions. These locations are named A and B and are placed along the half-way line of the serpentine turns. Location A corresponds to a location in the middle and location B shows the profiles near the exit of the fuel cell. The anode channel consists of a hydrogen and water vapor mixture and the cathode-side gas mixture consists of oxygen, nitrogen, and water vapor. The reaction characteristics of the fuel cell significantly depends on the humidity of the gases because the transport of protons depends on the local water content. For very low humidity, the reaction rates are lower than other inlet conditions studied.

The changes in density contours at the two locations of the fuel cell indicate the gas-composition changes. Water is produced on the cathode side and depending on the extent to which it equilibrates with the air stream, the mixture density decreases downstream as oxygen is consumed. The anode side shows a decrease in density from inlet to the mid-section of the fuel cell due to the consumption of hydrogen and the drag of water from anode to cathode by electro-osmosis. At downstream locations near the outlet, enough water is absent from the anode to create a strong back-diffusion of water vapor from the cathode side and therefore, the anode-side gas mixture density increases from the middle section.

In Fig. 3, the velocity vectors indicate both magnitude and direction of the flow in the planes perpendicular to the main flow channel. The flow predictions show both main flow and diffusion layer regions of the fuel cell. Note that the reference vectors are different for the cathode and anode flow regions to increase the readability. The size of the vectors shows that adjacent flow channels are significantly coupled with each other through the diffusion layer. Location A (Fig. 3(a)) shows that mass is consumed on the anode surface, but at location B (Fig. 3(b)) these vectors show that mass is injected to the anode-side flow. The strong vortex structures in the cathode-side flow channels indicate the presence of turns in the flow path. Though the plotted region is at the middle of two turns, the presence of upstream turns is reflected only in the cathode-side flow

Table 3
Different flow conditions used for different inlet humidity conditions

Inlet flow condition	Very low humidity	Low humidity	High humidity	Very high humidity
Observed average total current in A at 0.6 V [1,9]	2.3	4.8	6.5	4.2
Anode channel inlet				
Gas-mixture velocity	1.735	1.830	2.210	2.560
Mole fraction of H_2	0.96	0.94	0.86	0.79
Mole fraction of H_2O	0.04	0.06	0.14	0.21
Cathode channel inlet				
Gas-mixture velocity	3.665	3.995	4.525	6.45
Mole fraction of O_2	0.2	0.193	0.18	0.15
Mole fraction of N_2	0.763	0.735	0.69	0.56
Mole fraction of H_2O	0.037	0.072	0.13	0.29

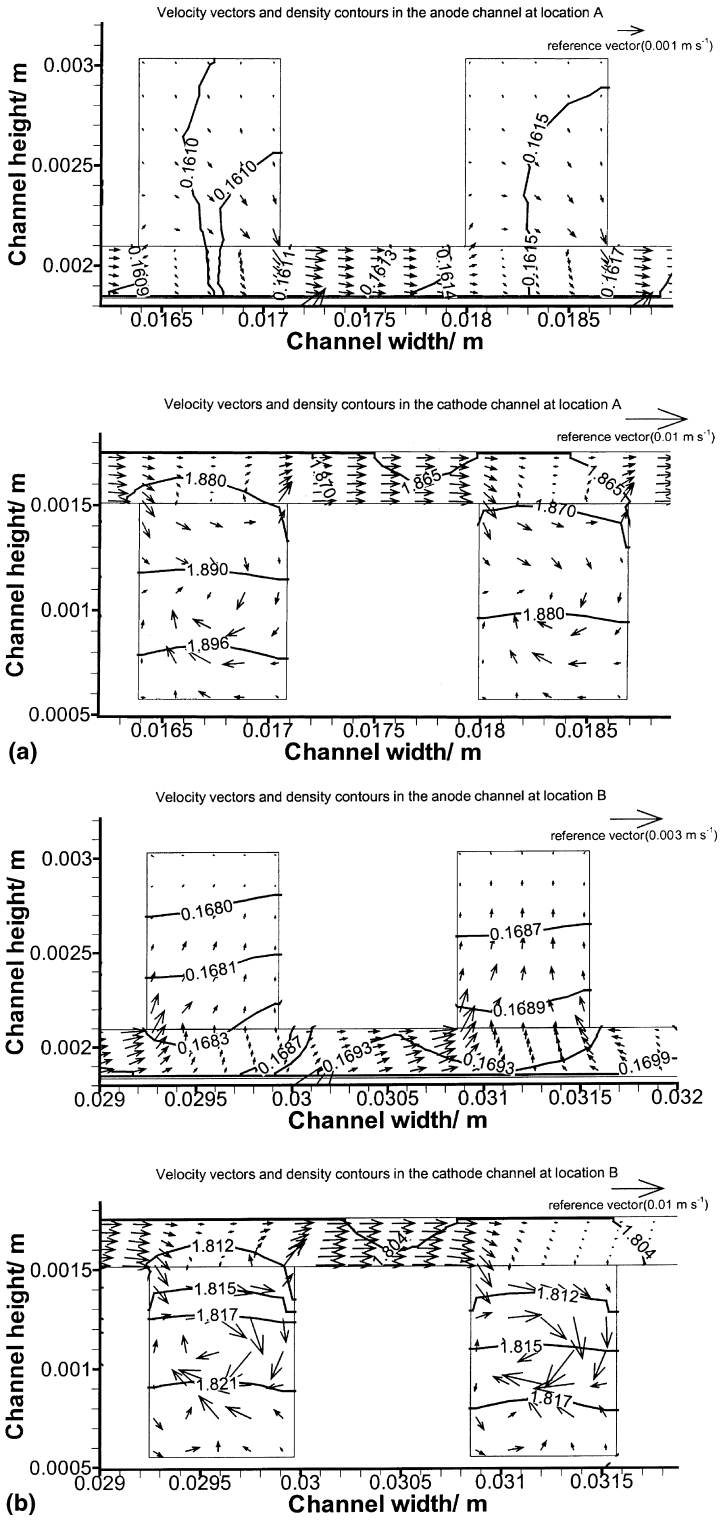

Fig. 3. (a) Velocity vectors and mixture density contours at location A for very low humidity; (b) velocity vectors and mixture density contours at location B for very low humidity.

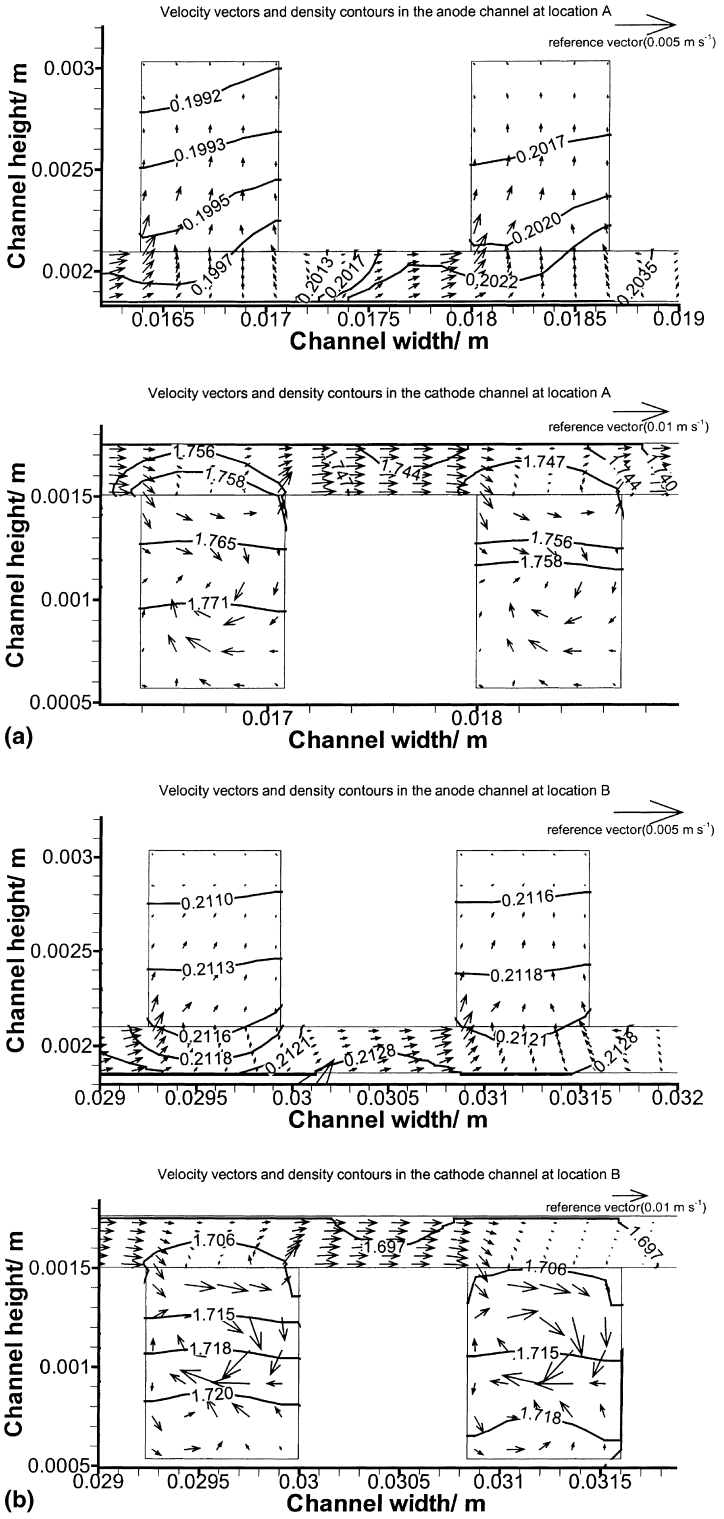

Fig. 4. (a) Velocity vectors and mixture density contours at location A for low humidity; (b) velocity vectors and mixture density contours at location B for low humidity.

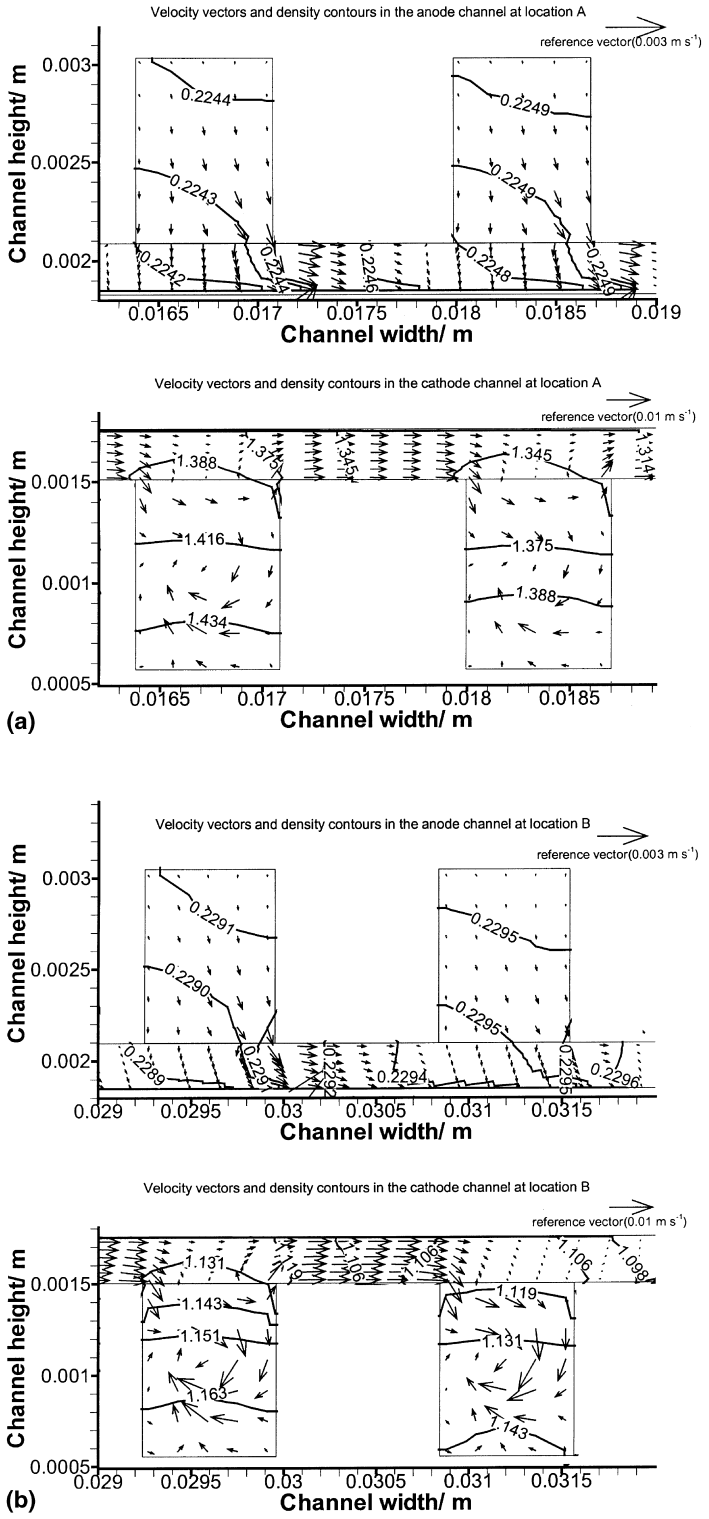

Fig. 5. (a) Velocity vectors and mixture density contours at location A for high humidity; (b) velocity vectors and mixture density contours at location B for high humidity.

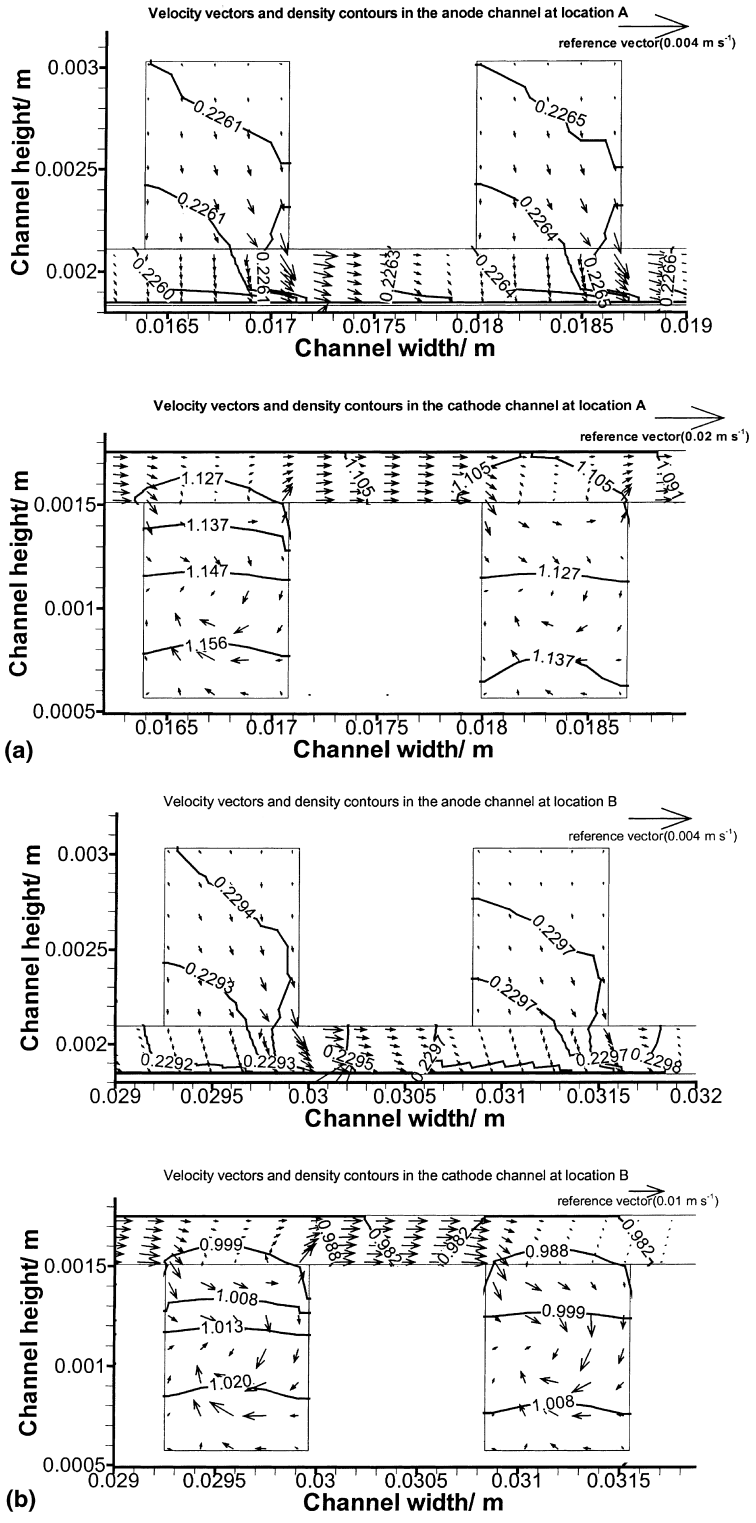

Fig. 6. (a) Velocity vectors and mixture density contours at location A for very high humidity; (b) velocity vectors and mixture density contours at location B for very high humidity.

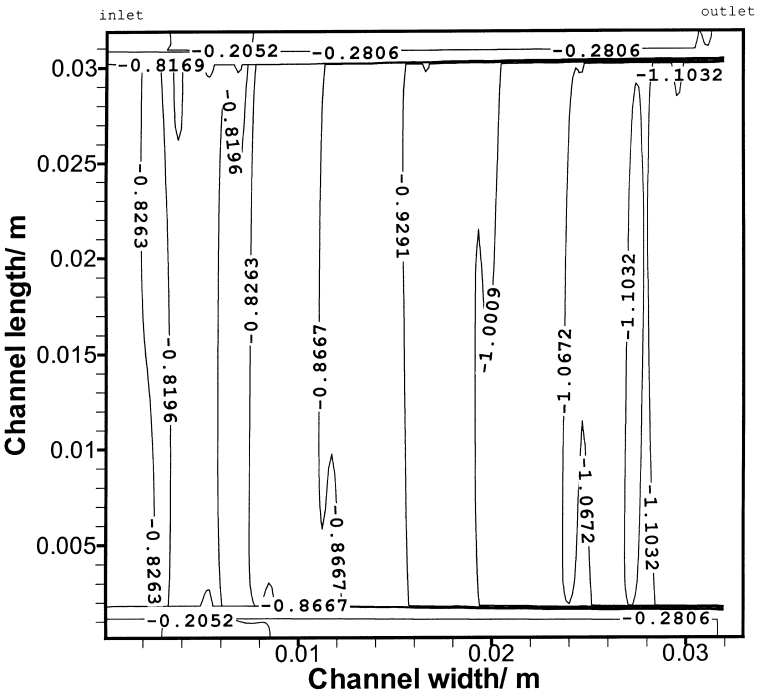

Fig. 7. The production pattern for hydrogen ($\times 10^{-11}$ kg/s) on the membrane surface of the anode side for low humidity conditions (a negative sign indicates consumption).

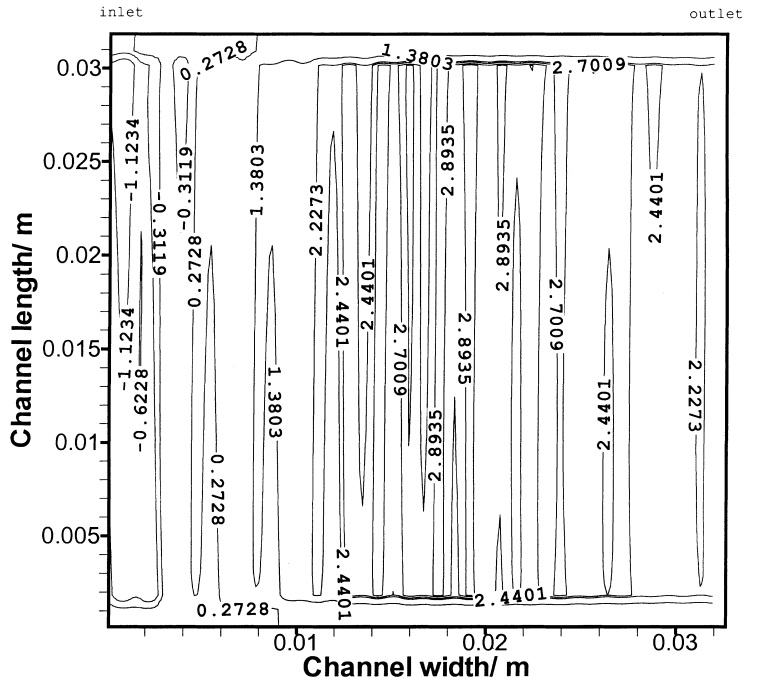

Fig. 8. Water production rate ($\times 10^{-11}$ kg/s) on the membrane surface of the anode side for low humidity conditions (a negative sign indicates consumption).

path. This is because of the fact that the velocity and mass flow rate of the cathode-side gas mixture is higher than that of the anode side due to the presence of an inert gas (nitrogen) in the gas-mixture.

Figs. 4(a) and (b) show the velocity vectors and density contours for the low humidity inlet condition. Note that the density contours are different from the previous set of figures. The change in density at the inlet is caused by the presence of higher amounts of water in the gas-mixtures flowing in both anode and cathode flow channels (e.g., compare Figs. 3(a) and (b)). Due to the greater water content in the anode gas-mixture, the reaction rates are more intense at the inlet. In the mid-region and near the outlet, the anode-side flow vectors show that back-diffusion is strong as evidenced by secondary flow going from the membrane to the main flow channel. Also, the cathode-side vectors indicate a strong flow through the porous layer.

Figs. 5(a) and (b) show the velocity vectors for the high inlet humidity and Fig. 6(a) and (b) show the velocity vectors and density contours for very high inlet humidity. Since presence of water enhances reaction rates, the density changes in the flow channels are stronger for these flow conditions. Note that the inlet velocities and mass flow rates change due to an increase in the water content in the mixtures and that different reference vectors are used in Fig. 6. It should be noted that the conditions of Fig. 6 correspond to a flooded MEA according to Lee et al. [9]. Local pressures indicate that the condensation of water is favorable at selected locations of the diffusion layer. This condensation can block the flow path as discussed in [1].

Figs. 7 and 8 show contours of the production rates of hydrogen and water vapor, respectively, on the anode surface of the MEA for the low humidity condition. Note that because hydrogen is consumed by the electrochemical reaction the sign is negative for these rates. On the other hand, water transport is governed by a delicate balance between electro-osmosis and back-diffusion processes and it may be transported from or to the anode side of the membrane. Fig. 7 shows that the rate of consumption is about 28% more near the outlet than the inlet. This can be explained by the water source–sink term shown in Fig. 8 which indicates that water is carried away from the anode stream to the cathode stream near the inlet but water is replenished by back-diffusion near the outlet for this low humidity conditions. More water is added to the anode stream and less hydrogen is consumed at the exit and therefore, the exit density and flow velocity are higher than at the anode inlet.

A graph of the oxygen consumption rates could be prepared by simply multiplying the values in Fig. 7 by a factor of eight according to the overall stoichiometry and the differences in the molecular weights of hydrogen

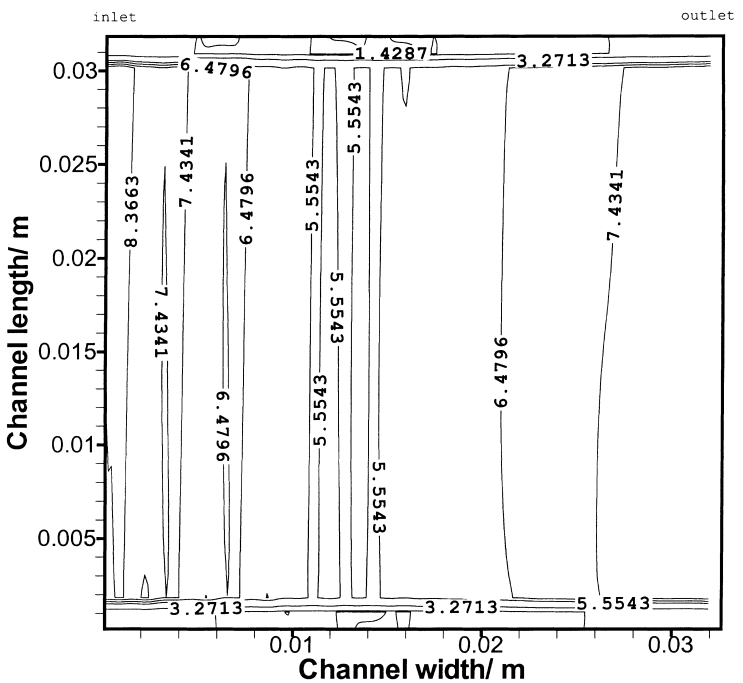

Fig. 9. Water production rate ($\times 10^{-11}$ kg/s) on the membrane surface of the cathode side for low humidity conditions (a negative sign indicates consumption). The source term combines chemical production of water and mass-exchange with the anode side of the membrane.

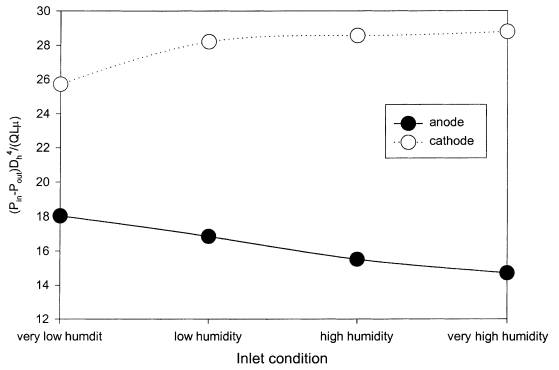

Fig. 10. Normalized pressure drop in the serpentine flow channels of the PEM fuel cell for different inlet humidity conditions.

and oxygen because they are coupled through the reaction current density. Fig. 9 shows the water production on the cathode side. Note that water is produced by the electro-chemical reaction and water is transported from anode to cathode by electro-osmosis and from the cathode to the anode by back-diffusion. This figure indicates the net mass balance of these three mechanisms of water transport.

Fig. 10 shows the normalized pressure drop characteristics in the serpentine flow channel. Eq. (24) in Table 2 was used to calculate the viscosity of the mixture. For a fully developed laminar channel flow, this normalized pressure drop is expected to be 652. Predictions show a significant flow cross-over from channel to channel through the diffusion layers, and therefore, pressure drop is lower than that expected for a regular channel flow. Since anode gas-mixture is thinner (contains mostly hydrogen), the pressure drop is lower in this channel compared to that in the cathode side.

4. Conclusions

A complete flow and mass transfer model is developed to simulate the inner details of a PEM fuel cell. The predictions provide detail flow patterns inside the flow channels that are difficult to measure. In the presence of electro-chemical reactions, hydrogen is consumed on the anode surface of the MEA and oxygen is consumed on the cathode side. These two gases react to produce water. Both anode and cathode gas streams are hydrated at the inlet to provide sufficient moistness to the MEA. The membrane does not allow gasses to permeate, only water migrates from one side to the other by electro-osmosis and diffusion processes. Results indicate that flow directions are significantly dependent on the mass consumption pattern on the MEA. A significant variation in gas-mixture density is also observed. Therefore, the computation technique for fuel cells should incorporate density variation effects in the calculation. The flow through porous diffusion layers is significant, and therefore, the overall pressure drop is lower than that expected in a serpentine channel.

Acknowledgements

This project was supported by the Department of Energy through Cooperative Agreement Number DE-FG02-91ER75666.

References

[1] S. Shimpalee, W.-K. Lee, S. Dutta, J.W. Van Zee, Predicting the 2-dimensional distribution of current density in a serpentine flow field PEM fuel cell, J. Electrochem. Soc., 2000, submitted.
[2] T.E. Springer, T.A. Zawodzinski, S. Gottesfeld, Polymer electrolyte fuel cell model, J. Electrochem. Soc. 138 (1991) 2334–2342.
[3] T.F. Fuller, J. Newman, Water and thermal management in solid-polymer-electrolyte fuel cells, J. Electrochem. Soc. 140 (1993) 1218–1225.
[4] T.V. Nguyen, R.E. White, A water and heat management models for Proton-Exchange-Membrane fuel cells, J. Electrochem. Soc. 140 (1993) 2178–2186.
[5] J.S. Yi, T.V. Nguyen, An along the channel model for proton exchange membrane fuel cells, J. Electrochem. Soc. 145 (1998) 1149–1159.
[6] J.S. Yi, T.V. Nguyen, Multicomponent transport in porous electrodes of proton exchange membrane fuel cells using the interdigitated gas distributors, J. Electrochem. Soc. 146 (1999) 38–45.
[7] V. Gurau, H. Liu, S. Kakac, Two-dimensional model for proton exchange membrane fuel cells, AIChE Journal 44 (1998) 2410–2422.
[8] S. Dutta, S. Shimpalee, J.W. Van Zee, Three-dimensional numerical simulation of straight channel PEM fuel cells, J. Appl. Electrochem. 30 (2000) 135–146.
[9] W.-K. Lee, J.W. Van Zee, S. Shimpalee, S. Dutta, Effect of humidity on PEM fuel cell performance, Part I: experiments, Proc. ASME Heat Transfer Div. 364 (1) (1999) 359–366.
[10] W.-K. Lee, C.H. Ho, J.W. Van Zee, M. Murthy, The effects of compression and gas diffusion layers on the performance of a PEM fuel cell, J. Power Sources, 1999.
[11] R. Bird, W. Stewart, E. Lightfoot, Transport Phenomena, Wiley, New York, 1960.
[12] S.V. Patankar, Numerical Heat Transfer and Fluid Flow, Hemisphere, New York, 1980.